university of groningen

University Medical Center Groningen

University of Groningen

# The shape of dark matter haloes - II. The GALACTUS H I modelling & fitting tool

Peters, S. P. C.; van der Kruit, P. C.; Allen, R. J.; Freeman, K. C.

*Published in:*
Monthly Notices of the Royal Astronomical Society

*DOI:*
10.1093/mnras/stw2099

**IMPORTANT NOTE: You are advised to consult the publisher's version (publisher's PDF) if you wish to cite from it. Please check the document version below.**

*Document Version*
Publisher's PDF, also known as Version of record

*Publication date:*
2017

Link to publication in University of Groningen/UMCG research database

*Citation for published version (APA):*
Peters, S. P. C., van der Kruit, P. C., Allen, R. J., & Freeman, K. C. (2017). The shape of dark matter haloes - II. The GALACTUS H I modelling & fitting tool. *Monthly Notices of the Royal Astronomical Society*, *464*(1), 21-31. https://doi.org/10.1093/mnras/stw2099

**Copyright**
Other than for strictly personal use, it is not permitted to download or to forward/distribute the text or part of it without the consent of the author(s) and/or copyright holder(s), unless the work is under an open content license (like Creative Commons).

The publication may also be distributed here under the terms of Article 25fa of the Dutch Copyright Act, indicated by the “Taverne” license. More information can be found on the University of Groningen website: https://www.rug.nl/library/open-access/self-archiving-pure/taverne-amendment.

**Take-down policy**
If you believe that this document breaches copyright please contact us providing details, and we will remove access to the work immediately and investigate your claim.

*Downloaded from the University of Groningen/UMCG research database (Pure): http://www.rug.nl/research/portal. For technical reasons the number of authors shown on this cover page is limited to 10 maximum.*

Download date: 04-05-2023

Monthly Notices
of the
ROYAL ASTRONOMICAL SOCIETY

MNRAS **464,** 21–31 (2017) doi:10.1093/mnras/stw2099

# The shape of dark matter haloes – II. The GALACTUS H I modelling & fitting tool

S. P. C. Peters,[1] P. C. van der Kruit,[1]★ R. J. Allen[2] and K. C. Freeman[3]

[1] *Kapteyn Astronomical Institute, University of Groningen, PO Box 800, NL-9700 AV Groningen, the Netherlands*
[2] *Space Telescope Science Institute, 3700 San Martin Drive, Baltimore, MD 21218, USA*
[3] *Research School of Astronomy and Astrophysics, The Australian National University, Cotter Road, Weston Creek, ACT 2611, Australia*

Accepted 2016 August 19. Received 2016 August 17; in original form 2015 July 23

## ABSTRACT

We present a new H I modelling tool called GALACTUS. The program has been designed to perform automated fits of disc-galaxy models to observations. It includes a treatment for the self-absorption of gas. The software has been released into the public domain. We describe the design philosophy and inner workings of the program. After this, we model the face-on galaxy NGC 2403 using both self-absorption and optically thin models, showing that self-absorption occurs even in face-on galaxies. These results are then used to model an edge-on galaxy. It is shown that the maximum surface brightness plateaus seen in Paper I of this series are indeed signs of self-absorption. The apparent H I mass of an edge-on galaxy can be drastically lower compared with that same galaxy seen face-on. The Tully–Fisher relation is found to be relatively free from self-absorption issues.

**Key words:** galaxies: haloes – galaxies: kinematics and dynamics – galaxies: photometry – galaxies: spiral – galaxies: structure.

## 1 INTRODUCTION

Modelling of the distribution and kinematics of neutral hydrogen in galaxies beyond our own and the most nearby systems M31 and M33 took off in the 1970s, with the addition of spectroscopic capability to the Westerbork Synthesis Radio Telescope (Allen, Hamaker & Wellington 1974). This new tool gave observers sufficient spatial and velocity resolution to resolve the H I structure and kinematics for a large number of galaxies. In edge-on galaxies, it thus became possible to trace the outer envelope of the position–velocity (*XV*) diagram in order to obtain the rotation curve of the galaxy (Sancisi & Allen 1979). Various strategies for this exist, such as fitting for the peak intensity or fitting a one-dimensional Gaussian with fixed velocity dispersion to the outer edge of the *XV* diagram (e.g. García-Ruiz, Sancisi & Kuijken 2002). We refer the reader to O'Brien, Freeman & van der Kruit (2010) for a detailed treatment of the various methods for deriving the rotation curve from an *XV* diagram.

For face-on galaxies, fitting the structure and kinematics was first done by modelling the zeroth and first-moment maps, based on the channel maps in the H I data cube. These gave rise to the famous spider diagrams, in which the isovelocity contours showed the mean velocity of the gas at each position in the galaxy (Rogstad & Shostak 1971). With the assumption of a thin disc, it is then possible to measure the rotation of the gas in rings centred on the galaxy. The position angle and inclination could be varied as a function of the rings. Assuming a rotation curve, Rogstad, Lockhart & Wright (1974) used it to model the peculiar velocity field of galaxy M83 and found the presence of a warp. Bosma (1978) improved this by minimizing line-of-sight velocity residuals for different rotation velocities in order to fit a rotation curve to the data. This method proved quite successful at modelling galaxies. It has been extended by many authors in many software packages (Begeman 1987; Schoenmakers 1999; Krajnović et al. 2006; Spekkens & Sellwood 2007). We refer to Józsa et al. (2007) for a detailed discussion on tilted-ring fitting to velocity fields.

The ever-continuing technological improvements led to ever higher-quality observations, which led to ever better-resolved galaxies, both spatially and in velocity. A natural consequence of this was the attempt to model the H I data cube itself. This was first attempted by Irwin & Seaquist (1991, 1993), who developed the CUBIT code.[1] CUBIT offers the user parametrized functions, which could be automatically fitted to the galaxy. The program was later expanded to fit more properties of galaxies (Irwin 1994).

Another software package is GALMOD, designed by T. S. van Albada and F. J. Sicking and incorporated into the GIPSY data reduction system (van der Hulst et al. 1992). Based on a tilted-ring geometry, GALMOD randomly projects a very large amount of 'clouds' into the H I data cube. As these clouds follow the specified kinematics and distribution, after sufficient samples have been drawn, the H I data cube has been built and the only task remaining is scaling the cube

★ E-mail: vdkruit@astro.rug.nl

[1] http://www.astro.queensu.ca/~irwin/

© 2016 The Authors
Published by Oxford University Press on behalf of the Royal Astronomical Society

Downloaded from https://academic.oup.com/mnras/article-abstract/464/1/21/2194606
by University of Groningen user
on 19 January 2018

to the desired intensity. GALMOD does not support automatic fitting and users thus have to fit a cube using the hand-and-eye strategy.

TiRiFiC [2] is another code that can automate the fit to a cube (Józsa et al. 2007). It is based on a tilted-ring model, but is expanded compared with GALMOD, to account for inhomogeneity in galaxy discs. Recently, it was used to fit features resembling spiral arms in edge-on galaxies (Kamphuis et al. 2013).

Finally, we note the GALAPAGOS project, which can automatically fit rotation curves in galaxies (Wiegert 2011). Out of all software codes currently publicly available, TiRiFiC seems to be the only one under active development. A fully automated three-dimensional fitting routine FULLY AUTOMATED TiRiFiC (FAT: Kamphuis et al. 2015) and another routine called $^{3D}$BAROLO that also estimates velocity dispersions (Di Teodoro & Fraternali 2015) have become available.

In Paper I (Peters et al. 2015a), we presented the H I observations for eight edge-on galaxies. One of the key conclusions of that article was that self-absorption could well play an important role. The effect of H I self-absorption has long been a topic of concern, for example in the work by Sancisi & Allen (1979) and that of Braun et al. (2009). The latter estimated quite significant corrections for self-absorption in the case of the Andromeda nebula M31. However, in most of the publications featuring models of neutral hydrogen in galaxies, the assumption remains that of an optically thin gas.

None of the above software packages supports modelling of self-absorption of the gas. This, combined with some other research questions we had concerning the neutral hydrogen, such as the behaviour of the velocity dispersion as a function of height above the plane, led us to develop a new tool for generating H I data cubes that could treat self-absorption. Rather than using a tilted-ring model, we model the galaxy as a single plane on which harmonic offsets above or below the central plane represent the warps. The code was developed in the PYTHON and C++ programming languages, with the computationally most intensive parts implemented as multi-threaded. The software is called GALACTUS. It has been publicly released under an open-source license and is listed in the Astrophysics Source Code Library as ascl.net/1303.018 (Peters 2013). The code can be downloaded at https://sourceforge.net/projects/galactus/.

The purpose of this article is twofold. In Section 2, we present the inner workings of GALACTUS. Section 3 discusses some important features of the tool in more detail. In Section 4, we explore the effective spin temperature in more detail. We test the program on face-on galaxy NGC 2403 in Section 5, using both optically thin and self-absorbing models. In Section 6, the fits from NGC 2403 are projected on to an edge-on galaxy to show that the maximum surface brightness profiles seen in Paper I should indeed have been higher. We test how self-absorption can lower the apparent total H I mass, depending on the inclination, in Section 7. The Tully–Fisher relation is shown to be independent of H I self-absorption in Section 8.

## 2 GALACTUS DESIGN

In this section, we discuss how GALACTUS generates a H I data cube. This generation consists of two steps. In the first phase the program creates a 3D model of the galaxy, while the second phase performs the radiative transfer.

To generate the model, the software creates a three-dimensional grid. The first two axes are aligned with and have the same lengths as the horizontal and vertical axes of the H I data cube channels.[3] The third axis does not denote velocity, but represents physical depth. The length of the third axis is the same as that of the horizontal axis of the H I data cube.[4]

Each position in this model is a three-dimensional pixel, also known as a volumetric pixel, or voxel for short. These voxels all represent a small volume of the galaxy. Since the voxels are perfectly aligned with the H I data cube channels, calculating the brightness of each pixel in a channel can be done by performing radiative transfer along the depth axis of the voxels associated with that pixel.

Each voxel is assigned coordinates $x$, $y$ and $z$. These are initially aligned with the horizontal, vertical and depth axes. We will subsequently bend and twist these coordinates to match the position and angle of the galaxy as seen in the cube. We emphasize, however, that these are *internal* coordinates; the grid of voxels itself does not change and *always* remains aligned with the H I data cube. The internal coordinates will represent the coordinate system of the galaxy in question.

### 2.1 Generating the galaxy coordinate system

We start with the coordinates $x$, $y$, $z$ assigned to the grid of voxels. As an aid to understanding the coordinate system, we illustrate the steps these equations perform in Fig. 1. We first shift the coordinates such that position (0,0,0) aligns with the centre of the model, i.e.

$$\begin{pmatrix} x \\ y \\ z \end{pmatrix} = \begin{pmatrix} x - \max(x)/2 \\ y - \max(y)/2 \\ z - \max(z)/2 \end{pmatrix}. \quad (1)$$

When performing a fit, the actual galaxy is often not perfectly aligned with the centre of the H I data cube. It is thus necessary to shift the coordinates, based on parameters $\mathrm{shift}_x$ and $\mathrm{shift}_y$:

$$\begin{pmatrix} x \\ y \end{pmatrix} = \begin{pmatrix} x - \mathrm{shift}_x \\ y - \mathrm{shift}_y \end{pmatrix}. \quad (2)$$

Next, the position angle $PA$ is applied. This is done using the coordinate transforms

$$\begin{pmatrix} x \\ y \end{pmatrix} = \begin{pmatrix} x\cos(PA) - y\sin(PA) \\ x\sin(PA) + y\cos(PA) \end{pmatrix}. \quad (3)$$

This is followed by the inclination $i$,

$$\begin{pmatrix} x \\ z \end{pmatrix} = \begin{pmatrix} x\cos(i) + z\sin(i) \\ -x\sin(i) + z\cos(i) \end{pmatrix}. \quad (4)$$

We can now convert to the final cylindrical coordinate system that will be used for the galaxy:

$$\begin{pmatrix} R \\ \theta \\ z \end{pmatrix} = \begin{pmatrix} \sqrt{x^2 + y^2} \\ \arctan(y/x) \\ z \end{pmatrix}. \quad (5)$$

Warps are known to exist in many galaxies, yet the actual physics is not well understood. The traditional way of dealing with warps is by applying a tilted-ring model. This is, however, impossible in our case, as the tilted-ring model does not map all coordinates to

[2] http://www.astron.nl/~jozsa/tirific/index.html

[3] Note that we assume the size of the pixel is not frequency-dependent. This is not true by default for H I data cubes created using MIRIAD.

[4] When modelling only one side of a galaxy, this length is doubled.



Downloaded from https://academic.oup.com/mnras/article-abstract/464/1/21/2194606
by University of Groningen user
on 19 January 2018

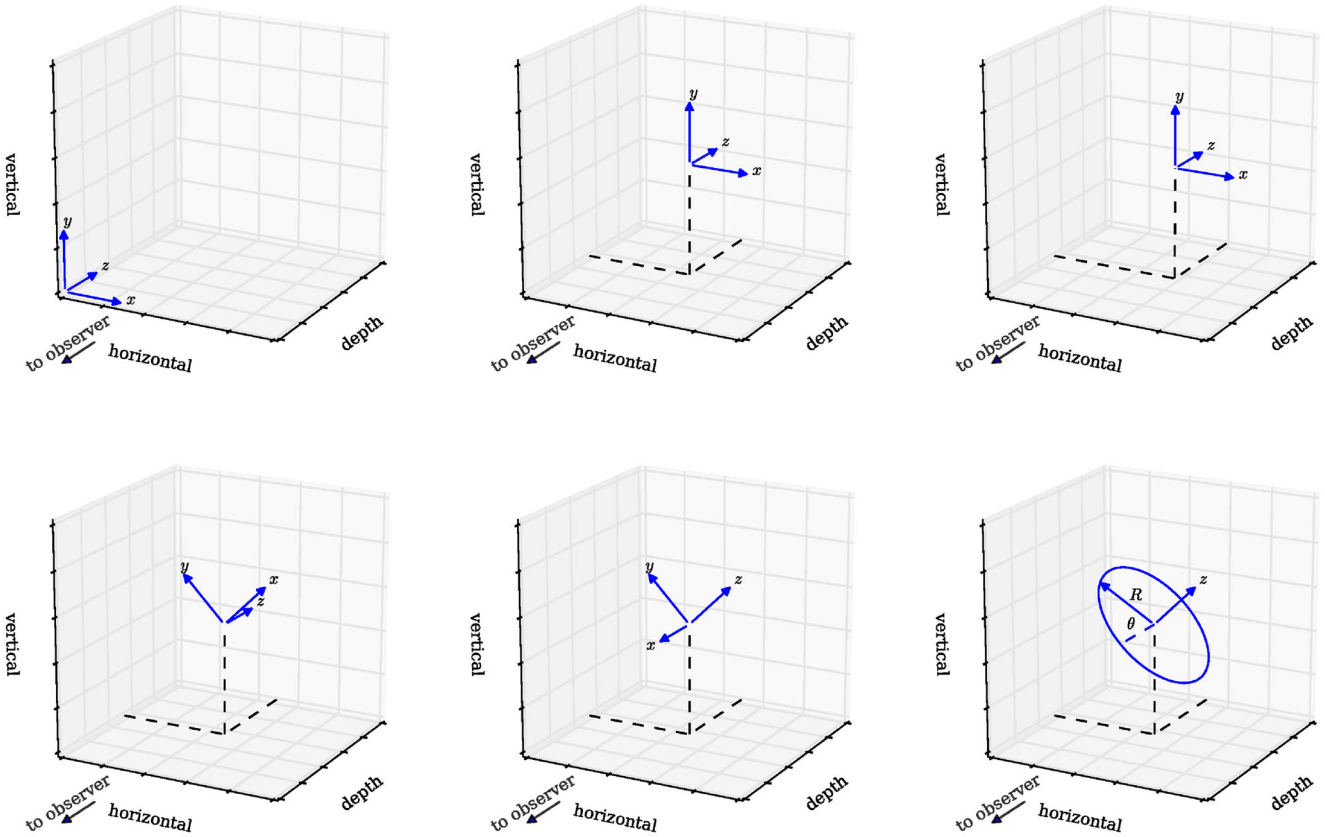


**Figure 1.** A schematic illustrating the generation of the galaxy coordinate system. The model demonstrate the generation of an edge-on galaxy at a position angle of 135°. The boxes on each side represent the outer edges of the voxels. From top left to bottom right: the initial coordinate system; centring the coordinate system (equation 1); the shift parameters can be used to move the central position of the galaxy along the horizontal and vertical axes (equation 2); the position angle is applied by rotating along the $z$ axis (equation 3); the inclination is applied by rotating along the $y$ axis (equation 4); in the final step, we switch to cylindrical coordinates.

a unique physical position. Some voxels would then be mapped to multiple values of $R$ simultaneously, which is undesirable.

We thus choose a different strategy to account for warps. Following Binney & Tremaine (1987), we define a warp as a harmonic oscillation along the disc, in which the mid-plane $z = 0$ is raised or lowered above the initial mid-plane as we go around the galaxy following $\theta$. The warp itself has a maximum amplitude described by superfunction $z_{\rm warp}(R)$ (see Section 2.6.1), which occurs at pitch angle $\theta_{\rm warp}$. We do not account for radial changes in pitch angle, so $\theta_{\rm warp}$ is a single value. Then

$$z = z + z_{\rm warp}(R) \times \cos(\theta + \theta_{\rm warp}). \quad (6)$$

### 2.2 Generating the physics

At this point, we have successfully generated the coordinates for the galaxy. The next step is to calculate the actual physical properties for each voxel. First, the line-of-sight velocity $v_{\rm obs}$ is calculated, based on rotation velocity $v_{\rm rot}$ and systemic velocity $v_{\rm sys}$. The rotation velocity $v_{\rm rot}$, along with the scaleheight of the disc $z_0(r)$, velocity dispersion $\sigma(R)$ and face-on surface density $A_{\rm HI}(R)$, are superfunctions, which are prepared by the user (see Section 2.6.1). Then

$$v = v_{\rm rot}(R) - L \times |\, z \,| \; (v \geq 0), \quad (7)$$

$$v_{\rm obs} = v \times \sin(\theta) \times \sin(i) + v_{\rm sys}. \quad (8)$$

Equation (7) offers the possibility to model lagging haloes. The lag is expected to decrease the observed rotation linearly, with value $L$, as the height $|z|$ above the plane increases. The model automatically prevents $v < 0$ and forces this to $v = 0$. When no halo lagging is modelled, $L$ is set to zero.

The observed velocity dispersion $\sigma$ is calculated separately for the three (cylindrical) directions $\sigma_{z,\rm obs}$, $\sigma[B_{R,\rm obs}]$ and $\sigma_{\theta,\,\rm obs}$ and then combined into a single observed velocity dispersion $\sigma_{\rm obs}$. The $a_R$, $a_z$, $a_\theta$ components are scalars, to account for a possible anisotropic velocity-dispersion tensor. There is currently no known case of anisotropy, so we set $a_R$, $a_z$, $a_\theta$ to one by default. We also correct for instrument broadening using dispersion $\sigma_{\rm inst}$, based on the channel width d$v$. Then

$$\sigma_{z,\rm obs} = a_z \sigma(r) \times \sin(\theta) \times \sin(i), \quad (9)$$

$$\sigma_{R,\rm obs} = a_R \sigma(r) \times \cos(i), \quad (10)$$

$$\sigma_{\theta,\rm obs} = a_\theta \sigma(r) \times \sin(i) \times \sin(\theta), \quad (11)$$

$$\sigma_{\rm inst} = {\rm d}v/2.355, \quad (12)$$

$$\sigma = \sqrt{\sigma^2_{z,\rm obs} + \sigma^2_{R,\rm obs} + \sigma^2_{\theta,\rm obs} + \sigma^2_{\rm inst}}. \quad (13)$$

The system takes the face-on surface density $A_{\rm HI}(R)$ and, using the flaring $z_0(R)$, converts it into a mid-plane density $\rho_{\rm m}(R)$. From this, the actual density $\rho$ for each voxel is calculated. We treat the gas

Downloaded from https://academic.oup.com/mnras/article-abstract/464/1/21/2194606
by University of Groningen user
on 19 January 2018

flaring as a Gaussian distribution. Alternative distributions exist, but the Gaussian has some advantages for the analysis of hydrostatics; see Paper V (Peters et al. 2015b). Based on Olling (1995), the errors due to this are expected to be minor. Then

$$\rho_{\rm m} = \frac{A_{\rm H\,I}(R)}{\sqrt{2\pi z_0(R)^2}}, \tag{14}$$

$$\rho = \rho_{\rm m} \exp\left[-\frac{z^2}{2\,z_0(R)^2}\right]. \tag{15}$$

The densities $\rho$ are all in units of H I atom cm$^{-3}$. In the final step, we convert to a local column density $N_{\rm H\,I}$ cm$^{-2}$ by multiplying by the physical length d$s$ that a single voxel represents along its depth axis:

$$N_{\rm H\,I} = \rho\,{\rm d}s. \tag{16}$$

### 2.3 Generating the H I data cube

We have now prepared the 3D cube and it is time to perform a ray-trace through the voxels along the depth axis and generate the final H I data cubes. GALACTUS supports two integration modes: optically thin and self-absorption.

#### 2.3.1 *Optically thin*

We assume that the H I follows a Gaussian velocity distribution:

$$N_{\rm H\,I}\,{\rm d}v = \frac{N_{\rm H\,I}}{\sqrt{2\pi\sigma^2}} \exp\left[-\frac{(v-v_{\rm obs})^2}{2\sigma^2}\right]. \tag{17}$$

For a single channel in the H I data cube, starting at velocity $v_{\rm l}$ and with a channel width d$v$, the number of atoms $N$ in a voxel that contribute to the emission in a single channel can be calculated as

$$N = \int_{v_{\rm l}}^{v_{\rm l}+{\rm d}v} N_{\rm H\,I}\,{\rm d}v. \tag{18}$$

We solve this integral using the error function *erf*, i.e.

$$N = \frac{N_{\rm H\,I}}{2\,{\rm d}v}\left[{\rm erf}\left(\frac{v_{\rm l}+{\rm d}v-v_{\rm obs}}{\sqrt{2\pi\sigma^2}}\right) - {\rm erf}\left(\frac{v_{\rm l}-v_{\rm obs}}{\sqrt{2\pi\sigma^2}}\right)\right]. \tag{19}$$

To calculate the optically thin surface brightness of each voxel, we use the optically thin limit of the radiative transfer equation (Draine 2011, Equation 8.26), i.e.

$$T_{B,{\rm thin}} = \frac{N}{1.8127\times10^{18}\,{\rm d}v}. \tag{20}$$

As there is no self-absorption, the intensity of a pixel can simply be calculated by taking the sum of $T_B$ in all voxels along the depth axis at the position of that pixel.

#### 2.3.2 *Self-absorption*

When running in self-absorption mode, the calculation becomes more complex. We follow the method from the previous subsection up to equation (20), which gives us the emitted temperature in the velocity range of the channel per voxel for an optically thin model. From this, we can then calculate the optical depth $\tau_\nu$ of that voxel, as[5]

$$\tau_\nu = T_{B,{\rm thin}}/T_{\rm spin}. \tag{21}$$

We assume that the galaxy has no internal continuum absorption, nor a background continuum source. This assumption is at least true for the galaxies in Paper I, although it does not hold for every galaxy. To calculate the brightness of a pixel, we begin with the voxel at the back of the depth axis associated with that pixel and calculate the radiative transfer equation with $T_{\rm bg} = 0$ (Draine 2011, equation 8.22):

$$T_{B,{\rm self-absorbing}} = T_{\rm bg}{\rm e}^{-\tau_\nu} + T_{\rm spin}\left(1-{\rm e}^{-\tau_\nu}\right). \tag{22}$$

For subsequent voxels, $T_{\rm bg}$ is the $T_B$ from the previous voxel. We continue this for all voxels along the depth axis until the final value $T_B$, which is adopted as the brightness for that pixel.

In our own Galaxy, many lines of sight are optically thick within a few hundred pc (Allen et al. 2012). To ensure sufficient accuracy, it is therefore advised to choose the physical length of each voxel along the depth axis such that it does not represent more than a hundred pc. This can be done using the accuracy parameter (see Section 3.2).

We note that the use of a constant spin temperature $T_{\rm spin}$ and a uniform density $\rho$ per voxel serves only as an approximation. In reality, the H I in galaxies consists of gas at a range of spin temperatures, not to mention varying densities (e.g. clouds), on scales much smaller than 100 pc. We discuss this in more detail in Section 4.

### 2.4 Beam smearing

After the H I data cube has been generated, we convolve the cube with the beam $\theta_{\rm FWHM}$. Note that we require the beam to be circular and the cells to be square.

### 2.5 Simulating noise

It is possible to introduce artificial noise into a cube. This can be done with the addition of the `-N` argument to the command-line call to GALACTUS. The noise $\sigma$ in table 3 of Paper I was measured as the standard deviation per pixel. In reality, however, the noise is correlated between neighbouring pixels due to beam smearing. GALACTUS automatically corrects for this, such that the noise $\sigma$ is equal to that measured from the standard deviation of the convolved field.

### 2.6 Input

GALACTUS can be used in two modes: stand-alone and as a software library. To obtain the stand-alone version, the user can download the source code of the program from the dedicated website at sourceforge.net/p/galactus. After compiling the required C++ libraries, the program can then be run from the program folder using the command `./Galactus ini-file`. GALACTUS uses ini files as its main source of information and any run of the program thus needs to be set up using them. We provide a list of all the options in the online Appendix.

[5] Note that this is just a rewrite of equation (20) with equation (8.11) in Draine (2011).


Downloaded from https://academic.oup.com/mnras/article-abstract/464/1/21/2194606
by University of Groningen user
on 19 January 2018

It is also possible to import GALACTUS into your own PYTHON programs as a library. All libraries required to run the program are contained in the `support/` module. It is beyond the scope of this article to discuss this in detail and we refer to the documentation in the code itself for more details. In short, to generate a basic model, a programmer would first need to import the `Galaxy` class from the `support.parameters` module, initialize a version of it and then use the `parse_ini(filename)` method to initialize all parameters in the `Galaxy` object. The H I data cube can then be generated by calling the `support.mainmodel.model()` method. The source code has been extensively documented and we invite developers to have a look and contribute to the code base.

#### 2.6.1 *Superfunctions*

While most variables in GALACTUS are single-valued, the rotation curve and face-on surface density are examples of so-called superfunctions. Superfunctions are a special class of functions that can behave differently based on the preference of the user. In their '1' or '2' modes (see Section A, Appendix), they act as parametrized functions, while in the '3' and '4' modes they act as tabulated functions. In tabulated mode, the user specifies the values that the function holds at positions $R$. During runtime, GALACTUS performs a linear interpolation over these points to calculate the values of intermediate radii. We have experimented with alternative types of interpolation, such as spline interpolation. While favourable from a theoretical point of view, in practice we found that during fitting a spline could start to show extreme spikes (both negative and positive) in an attempt to still reach all the user-specified $R$ and $f(R)$ values. This made attaching boundary conditions very hard. In the end, we settled for linear interpolation between values.

In parametrized mode, the functions are simplified to an analytical form that best fits their common profiles. For example, the velocity curve $v_{\rm rot}$ has a parametrized form of $v_{\rm rot}(R) = a + a/(R/b + 1)$. The advantage of parametrizing functions is that it limits the amount of free parameters, in this case only two. The form of each superfunction is shown in Table A, Appendix. Another advantage to parametrized functions is that they are less sensitive to noise – although at the expense of accuracy – and give the ability for a very quick first estimate of the parameters. We provide a function `all_to_spline`, which can convert parametrized curves to tabulated ones.

### 2.7 Output

GALACTUS is capable of producing a range of products, which can be selected in the parameter file. The main output of the program is the generated H I data cube. There are more options, however. In this subsection, we will highlight the most important ones.

#### 2.7.1 *Total, visible and hidden matter cube*

Since the brightness can depend on opacity, the generated H I data cube no longer represents the total amount of atoms. The total matter cube gives the total amount of atoms in a velocity range, before any self-absorption is applied. This starts with the result of equation (19), which is a cube with the amount of H I per voxel for a given channel. Rather than converting the data into temperatures with equation (20), we instead sum the voxels along the depth axis and thus obtain the number of atoms. This process is repeated for each channel in the H I data cube.

In contrast, the visible matter cube uses the generated H I data cube and converts it back into atoms, using the inverse of the optically thin approximation from equation (20). When running in optically thin mode, the visible and total matter cubes are equal. The difference comes into play when running in self-absorption mode. This difference can be visualized with the hidden matter cube, which is a cube showing the difference between the total and visible matter cubes.

#### 2.7.2 *Moment maps*

Besides channel maps, GALACTUS can also output various moment maps: specifically the zeroth, first, second and third moments. These follow the same moment definitions as GIPSY (van der Hulst et al. 1992).

#### 2.7.3 XV *map and integrated profile*

GALACTUS is also capable of plotting the integrated *XV* (otherwise known as integrated Position-velocity) diagrams of the H I data cube, by integrating the generated H I data cube along the vertical axis. By also integrating along the velocity axis, the program can generate an integrated profile.

### 2.8 Fitting

Fitting a galaxy model to a H I data cube is a very complex problem and great care needs to be taken in order to fit the data properly. To give the user the best capabilities, we have included a number of fitting routines in the program. Suppose one is fitting a well-resolved face-on galaxy with fixed velocity dispersion and no beam smearing. In this case, a line of sight corresponds to a single radius inside the galaxy. This radius is sampled by many pixels as we look around the galaxy. The parameter space is thus very limited, as each radius only has to fit a single face-on surface density and rotation curve. A simple fitting routine, such as the Levenberg–Marquardt algorithm (Press et al. 1992), can quickly converge to the optimal solution. We make use of the SCIPY package `optimise.leastsq`.

When beam smearing is involved, the light from various radii starts to overlap, which causes the parameter space to become far more complex. Even worse, local optimal solutions start to appear. For example, where the true face-on surface density at a radius might be $5 \times 10^{20}$ atom cm$^{-2}$, the model could be happily converging towards $3 \times 10^{20}$ and $7 \times 10^{20}$ atom cm$^{-2}$ in two adjacent radii, with the beam taking care of the smoothing back to $5 \times 10^{20}$ atom cm$^{-2}$ on average. The velocity dispersion also creates many local optima, especially in edge-on galaxies, where the use of a very high velocity dispersion at a high radius $R$ can mask out the velocity dispersion at a slightly lower radius, thus convincing the program that low velocity dispersions at that radius are also acceptable.

To find the global optimum, a more powerful algorithm is required. We have tested many algorithms extensively. Our preferred method is the PSWARM algorithm, which is a combination of pattern search and particle swarm (Vaz & Vicente 2007, 2009; Thi, Vaz & Vicente 2012)[6] and is used through the OPENOPT framework.[7] Solving for a global optimization problem requires a far more thorough search of the parameter space and thus requires much more time to converge, compared with the Levenberg–Marquardt algorithm. We

[6] www.norg.uminho.pt/aivaz/pswarm/
[7] Available at https://pypi.python.org/pypi/openopt



Downloaded from https://academic.oup.com/mnras/article-abstract/464/1/21/2194606
by University of Groningen user
on 19 January 2018

have also tested various implementations of genetic algorithms, but found that the random nature of the improvements led to unacceptably long convergence times.

We also find that, when fitting for the velocity dispersion, it is often misused by an algorithm to 'average over' local structure in the *XV* diagram by using a very high velocity dispersion. This can happen in particular when warps and self-absorption are present, but are not allowed for in the modelling. In those cases, it is not even possible to model the *XV* diagram accurately. The algorithm will then start to misuse the velocity dispersion.

To estimate the $\chi^2$ cost of some parameter set $p$ on the model $T_{\rm model}(p)$, we use least-squares deviations. We show this in equation (23), where we use the standard deviation of the noise $\sigma$ from the observed H I data cube $T_{\rm observation}$. Index $i$ runs over all pixels in the H I data cube:

$$\chi^2(p) = \sum_{i=0}^{N_{\rm pixels}} \frac{[T_{\rm model}(i;p) - T_{\rm observation}(i)]^2}{\sigma^2}. \quad (23)$$

Lastly, we implement a Monte Carlo Markov Chain (MCMC) version of the model. MCMC is a different approach to model optimization. Rather than look for a single parameter set that represents the global optimal solution, MCMC explores the parameter space and draws samples of parameter sets from the region where, based on the probability distribution, the optimum is expected. We make use of the EMCEE library (Foreman-Mackey et al. 2013), which implements the affine-invariant ensemble sampler proposed by Goodman & Weare (2010). Following the cost function $\chi^2$, given in equation (23), the log-likelihood $\mathcal{L}$ function for a particular parameter set $p$ is calculated as

$$\mathcal{L}(p) = \log\left(-\frac{\chi^2(p)}{2}\right) \quad (24)$$

$$= \log \sum_{i=0}^{N_{\rm pixels}} -\frac{[T_{\rm model}(i;p) - T_{\rm observation}(i)]^2}{2\sigma^2}. \quad (25)$$

EMCEE uses multiple MCMC samplers in parallel, each of which generates a chain of samples. For the number of samplers, we choose double the amount of free parameters, which for tabulated fitting implies 150–300 chains. After a sufficiently long burn-in period, we collect a large group of $N$ samples from the collection of chains. For each free parameter that is being fitted, the group thus has $N$ values that this parameter would most likely have. These values thus form a distribution. In this and subsequent articles, we make use of the central 68, 95 and 99.7 per cent of the likelihood distribution to denote the errors. Note that if the distribution in a parameter follows a Gaussian distribution, this would be equal to the 1-, 2- and 3$\sigma$ deviations of that Gaussian.

## 3 NOTES

### 3.1 Masking the data

GALACTUS can deal with masked pixels. Pixels that are masked in the input H I data cube, specified with the `image` parameter (see also Section A, Appendix), are treated as pixels with a value of zero. GALACTUS will still render the corresponding pixels in the output model, as the user could still be interested in the model at these pixels, but has masked them on purpose for some reason.

The `mask` parameter can be used to specify which pixels GALACTUS does not need to render. The parameter needs to point to a H I data cube, which can be the same as the one used in the `image` parameter. All pixels in the channel maps that make up the H I data cube that have value NaN[8] are selected as the masked pixels. GALACTUS calculates which voxels contribute to which pixels. If a voxel contributes only to masked pixels, it is removed from the calculation. This can lead to drastic performance increases.

The last type of mask is the `boundaries` mask. This can be used to specify in which channel maps the line-of-nodes velocity $v_{\rm rot}(R)$ is expected to lie. It is then possible to mask everything except the outer envelope of an *XV* diagram. The fitting algorithms are then constrained in the $v_{\rm rot}(R)$ parameter.

### 3.2 Concerning the resolution

By default, GALACTUS traces only one ray per pixel. The initial cube has voxels that are one pixel wide on all sides. Thus, if the output cube has pixels with a (projected) size of 1 kpc, the voxels are 1 kpc on each side as well and the ray is thus sampled every 1 kpc as it crosses the galaxy. For a galaxy that has a diameter of 20 kpc, the rays will thus at sample most only 20 positions inside the galaxy. This can lead to a jagged-looking result.

To provide a better representation of the galaxy, we have introduced two additional user options. The first is the `accuracy` level, which controls the number of samples along the ray. It works as a scalar on the original number of samples along the depth axis, such that, if one originally measured 20 samples, an accuracy level of four would lead to 80 samples. Following the above example, these would thus be separated 250 pc apart along the ray.

The second option is *supersampling*, a technique common in the 3D graphics industry. In supersampling, each output pixel is represented by multiple rays at slightly different positions inside the pixel, with the result being the average of all rays. For example, suppose the original ray runs a trace centred on the middle of the pixel, thus at position 1/2. Then, with supersampling, we have two rays, at both 1/3 and 2/3. Suppose that a significant change would occur beyond position 1/2. The normal model would not represent this, while a supersampled pixel would. Supersampling works in both the horizontal and vertical directions. A supersampling of factor two means each pixel is sampled by four rays.

An increased accuracy thus increases the number of voxels along the depth axis. An increase in supersampling decreases the size of an individual voxel along the horizontal and vertical axis and thus increases the number of voxels quadratically. The increases in accuracy and supersampling are thus increases in the number of voxels that need to be calculated, which come with a performance penalty. It is thus important to realize that there is a trade-off between the desired accuracy and the time available.

In Fig. 2, we visualize this trade-off. We show the timing results of an edge-on model, at multiple combinations of supersampling and accuracy levels, with their relative error compared with a very high-resolution model with an accuracy of five and a supersampling of five, which in this case implies a model with voxels that each represent 27 pc on all sides. In a perfect world, the accuracy and supersampling could be set to $\infty$ and the results would be perfect. In practice, however, due to time constraints, there is no single right setting; it is thus important to think about the problem and decide what the best setting should be. For example, in a face-on galaxy, one quickly runs the risk of 'overshooting' the disc, if there were

[8] NaN stands for 'Not A Number'. By default, MIRIAD masking gives pixels this value.


Downloaded from https://academic.oup.com/mnras/article-abstract/464/1/21/2194606
by University of Groningen user
on 19 January 2018

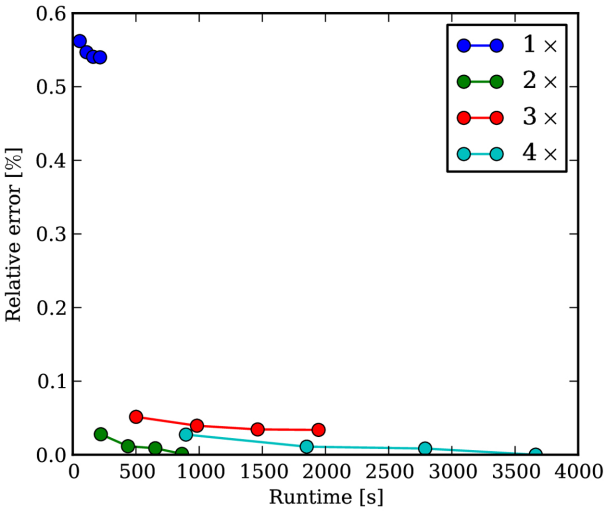


**Figure 2.** Accuracy versus time trade-off visualized. The various tracks show the various supersampling modes, while the dots along each track represent the accuracy level used. Along each track, the top left point is always an accuracy level of one, progressing to an accuracy level of four at the right-hand side. Overall, the rule holds that the closer to (0,0) the better.

not enough samples along the ray, and a higher accuracy would then be desirable. In an edge-on, overshooting the disc is less important, but one might want to supersample the galaxy so as to model the vertical structure more accurately.

A supersampling of two incorporates a special feature, which positions the four rays in an optimal distribution. In this way, both the horizontal and vertical axis of the pixel in question are traced at four unique positions, rather than the default of two positions per axis. The effect of this can be seen in Fig. 2, where the results from a supersampling of two are nearly equal to the far more computationally expensive supersampling of four (i.e. 16 rays). A supersampling of two outperforms a supersampling of three. Fig. 2 also demonstrates that increasing the accuracy does not improve the model drastically. We recommend that the accuracy be chosen such that the length of the voxel along the depth axis is at most 100 pc, such that the radiative transfer equation is calculated with sufficient precision.

## 4 THE EFFECTIVE SPIN TEMPERATURE

In a real galaxy, H I never has a single spin temperature. The gas is balanced between the phases of the Cold Neutral Medium (CNM), which has a median spin temperature of 80 K, and the Warm Neutral Medium (WNM), with temperatures between 6000 and 10 000 K. The fraction of the mass contained in either state remains unclear, but it was estimated that 40 per cent of the neutral hydrogen mass of the Galaxy is in the CNM (Draine 2011).

With such a wide range in temperatures, how reliable is the use of a single effective spin temperature? To test this, we have run a range of Monte Carlo simulations. For a fixed CNM fraction $p$, we calculate the effective spin temperature over a range of column densities. For column density $N_{\rm H\,I}$, we divide the sample up into $N_{\rm clouds}$ equal sized bins, each of which represents a cloud of gas with a column density $N_{\rm cloud}$. The number of clouds is randomly picked between 100 and 1000, to represent the variation in crossing a real galaxy. Based on fraction $p$, we randomly choose if a cloud is part of either the CNM or the WNM. If it is a CNM cloud, it is assigned a random spin temperature $T_{\rm spin}$, chosen from a uniform distribution between 50 and 100 K. Otherwise, it is assigned a $T_{\rm spin}$ chosen from a distribution between 6000 and 8000 K. We then perform a line-of-sight integration, starting with background temperature $T_{\rm bg} = 0$ K, using equations (20), (21) and (22).

Taking 1000 samples at each column density $N_{\rm H\,I}$, we obtain a distribution of observed temperatures $T_B$. We show the results for two mass fractions in Figs 3(a) and (b). We fit a single effective $T_{\rm spin}$ to the median of the distributions, using

$$T = T_{\rm spin}\left(1 - {\rm e}^{-\tau}\right). \quad (26)$$

The results are overplotted in red in Figs 3(a) and (b). For the 40 per cent fraction, we find an effective spin temperature of 177.2 K, while for the 80 per cent fraction we find 89.5 K. Clearly, the balance between the two populations is important. More importantly, in both cases we see that the median spin temperature levels out and a single effective spin temperature gives a decent fit to the median one. Provided the right value is chosen, it is thus possible to use a single effective spin temperature when modelling a galaxy. The exact value for this effective spin temperature is hard to determine and beyond the scope of this work. During fitting, we will use a spin temperature of 100 K, a value in good agreement with the figures in Paper I.

## 5 FACE-ON GALAXY NGC 2403

In the following sections, we test the program for a number of cases. To begin with, we wish to test our fitting routines on a face-on galaxy to confirm the accuracy of the rotation curve and surface density modelling. For this purpose, we have chosen the galaxy NGC 2403. Like the galaxies in our sample, it is a nearby, late-type Scd galaxy (Tully & Pierce 2000). H I observations of high spatial and velocity resolution are available for it. Even though the rotation velocity is slightly higher (130 versus 90 km s$^{-1}$ on average), it is suitable for comparing with our sample of edge-on, late-type galaxies (Paper I). Using the tip of the red giant branch, Dalcanton et al. (2009) estimated the distance at 3.2 Mpc. The H I kinematics have have been studied in detail by Sicking (1997), Fraternali et al. (2001, 2002) and de Blok et al. (2008). The galaxy is part of the public data release from The H I Nearby Galaxy Survey (THINGS), which was based on B-, C- and D- configuration Very Large Array (VLA) observations[9] (Walter et al. 2008). The THINGS observations were previously studied in detail by de Blok et al. (2008), who measured a systemic velocity $v_{\rm sys}$ of 132.8 km s$^{-1}$ and an inclination $i$ of 62.°9.

We test GALACTUS using the naturally weighted H I data cube from the THINGS website. The original cube has a size of 2048 × 2048 pixels and 61 channels, which is too large for GALACTUS to handle. MIRIAD task `smooth` was used to create a circular beam with a full-width at half-maximum (FWHM) of 12.4 arcsec. We used the task `regrid` to downsize the resolution from 1.0 to 8.8 arcsec pixel$^{-1}$, resulting in somewhat less than 2 pixel beam$^{-1}$. The initial beam was 8.75 × 7.65 arcsec$^2$, with a position angle of 25.2°. We used the task REGRID to downsize the sampling of the data from 1.0 to 8.8 arcsec pixel$^{-1}$, resulting in somewhat less than 2 pixel beam$^{-1}$. We have chosen this sampling as this corresponds to roughly 100 pc per pixel. As each pixel is supersampled by four rays, the area of the FWHM of the beam will be modelled by the order of 20 rays, which is sufficient to prevent undersampling. While an even higher resolution would have been desirable, it was found

[9] The public data from the THINGS survey is available at http://www.mpia.de/THINGS/Data.html



Downloaded from https://academic.oup.com/mnras/article-abstract/464/1/21/2194606
by University of Groningen user
on 19 January 2018

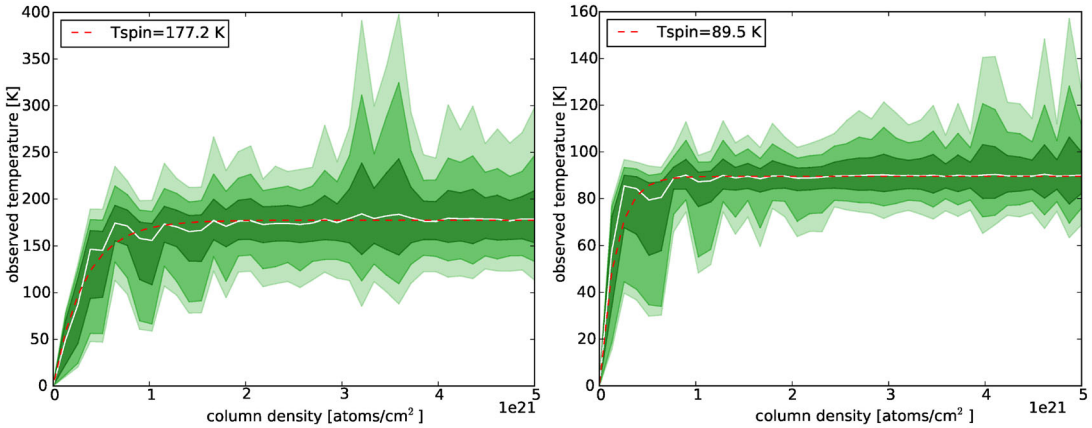


**Figure 3.** Effective spin temperature assuming 40 per cent (left panel) or 80 per cent (right panel) of the gas is in the CNM. Colour bars represent 68.5, 95.45 and 99.73 per cent of the distribution at each point. The 50 per cent (median) of the sample is shown in white. The dashed line (red online) represents the fitted effective spin temperature.

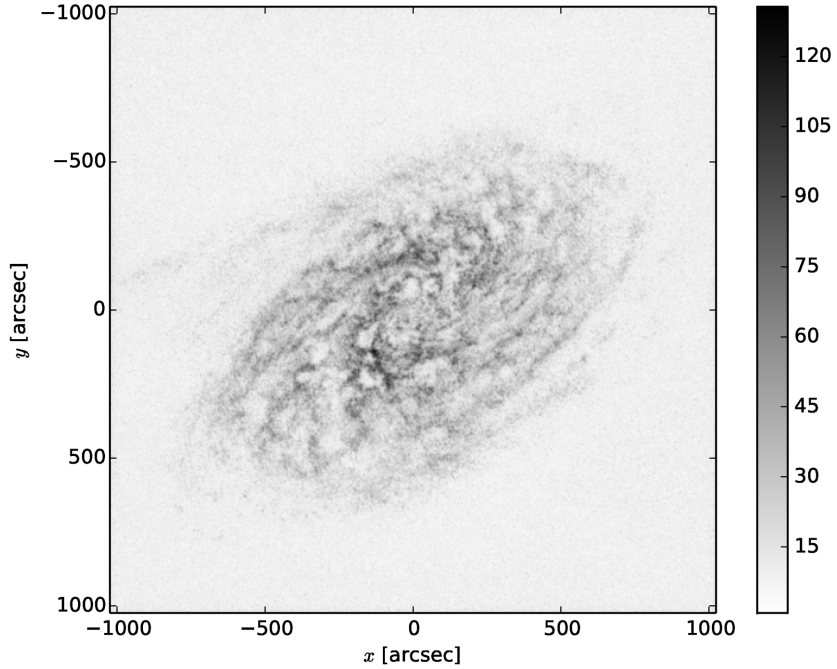


**Figure 4.** Maximum surface brightness map for NGC 2403. The values for the bar on the right denote brightness temperature in K.

to be computationally infeasible, as the required memory and computation time increase by a power of three. Using task `cgcurs`, a mask was drawn by hand around all regions containing flux. With task `imsub`, we used this mask to create a final, masked cube that only contains parts of the cube where flux was detected. The final cube has a size of 232 × 228 pixels and 55 channels at 5.169 km s$^{-1}$ resolution.

In Fig. 4, the maximum surface brightness has been calculated from the original THINGS image. Here we have converted the intensity $I$ from Jy beam$^{-1}$ to K using equation (4) of Paper I:

$$T_B = \frac{\lambda^2 S}{2k_B \Omega} = \frac{606\,000\, S}{\theta^2}. \quad (27)$$

A clear spiral structure is visible in the figure. Most of the brightness hovers between 45 and 60 K and appears as spiral arm structure, with local regions peaking at over 120 K. We rotated the galaxy such that the major axis is lined up with the horizontal $x$-axis. If we only look at the maximum brightness along the horizontal axis, such that each position reflects the maximum brightness independent of location along vertical axis, we obtain the result seen in Fig. 5. This produces a result similar to the maxima along the major axis in edge-on galaxies as seen in Paper I. There, we found a plateau around 80 K in all edge-on galaxies for a significant part of their discs. There is no clear plateau in Fig. 5. The wings of this profile are much extended, running continuously towards the background. This is different compared with our edge-on galaxies, where we observed very sharp wings. In Paper I, we argued that the plateau in the profile was due to self-absorption in long lines of sight. The shorter lines of sight in NGC 2403 would therefore not be expected to exhibit (strong) signs of self-absorption. Only in the dense inner region do the densities still reach levels high enough for self-absorption to affect them significantly, as exhibited by the peak around 80 K.


Downloaded from https://academic.oup.com/mnras/article-abstract/464/1/21/2194606
by University of Groningen user
on 19 January 2018

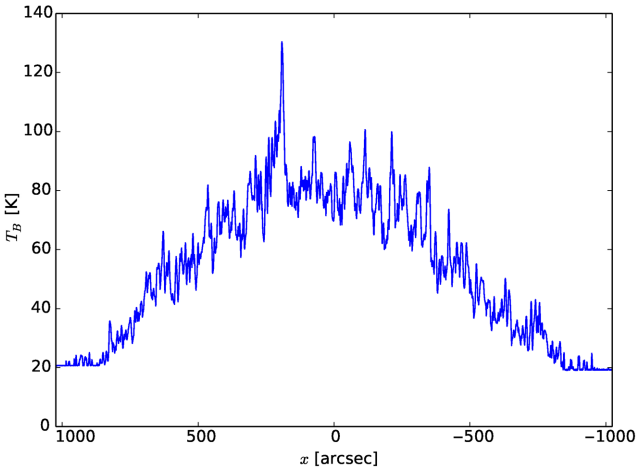


**Figure 5.** Radial maximum surface brightness of NGC 2403.

We thus argue that, with the exception of the central part, most of the galaxy is not affected by significant self-absorption. We note in general that observations of self-absorption can only occur when the beam has sufficient spatial resolution. Otherwise, the effect will wash out due to smearing.

We fit NGC 2403 using both an optically thin model and a self-absorption model. For the self-absorption model, we use a spin temperature $T_{\rm spin}$ of 100 K. We fit the galaxy using a constant velocity dispersion of 10 km s$^{-1}$. We constrain the disc to a thickness of 700 pc in the inner part, flaring out to 1 kpc at 1400 arcsec (23 kpc). Warps or lagging haloes are beyond the scope of the current test. A double-pass strategy is used to fit the data. We first use the parametrized functions for the face-on surface density, flaring and rotation curve. This pass is fitted using the Levenberg–Marquardt algorithm. After that, we interpolate over the fitted functions and tabulate them into 37 chunks with a separation of 38 arcsec. We then run a second pass. As the galaxy is face-on and very well resolved, there is no strong danger of running into local minima and we thus again use the quick Levenberg–Marquardt algorithm.

The results for this fitting are shown in Fig. 6. The rotation curves of the optically thin and self-absorbing fits are effectively identical. It is reassuring to find that in both cases the same rotation curve is found, proving that the observed $v_{\rm rot}$ in face-on galaxies is not affected by self-absorption. The profile also matches up well with the profile from Sicking (1997). Only in the outer radii do we suffer more from signal-to-noise issues. Given the detailed tilted ring and warp fitted by Sicking (1997), which we are ignoring, this is expected.

Now consider the mass models. Unsurprisingly, the optically thin profile is clearly lower than the optically thick profile. The first has a total mass of 2.9 × 10$^9$ M$_\odot$. The self-absorbing mass totals 3.2 × 10$^9$ M$_\odot$, of which ∼10 per cent is hidden by the self-absorption. The overall shape of the profiles agrees well, with all local features visible in both profiles. In comparison, Sicking (1997) found slightly more mass than our optically thin model. They report a total mass of 3.27 × 10$^9$ M$_\odot$ for NGC 2403.

## 6 THE MAXIMUM SURFACE BRIGHTNESS IN AN EDGE-ON GALAXY

In Section 3 of Paper I, we presented a simple toy model to demonstrate that a plateau of constant maximum surface brightness is an indication of self-absorption. Using GALACTUS, we can now extend this toy model to a more physical basis. We project the previous fit of NGC 2403 to a full edge-on orientation. We use the self-absorption fit as the face-on surface-density and rotation curves as input parameters (see Fig. 6). We will compare an optically thin model and a self-absorption run at a spin temperature of 100 K.

The results for this test are shown in Fig. 7. The model for the galaxy at its original inclination peaks at roughly 40 K (blue line). This is lower than the observed maximum brightness maps as seen in Fig. 5. This is expected, as the model cannot recreate the small-scale bright regions seen in the actual observation. When we rotate the galaxy to full edge-on, we see that the long lines of sight carry the integration well above 300 K (green line). Especially near the inner part at $x = 0$, the model keeps rising. As we have argued in Paper I, this is never observed. Comparing this with

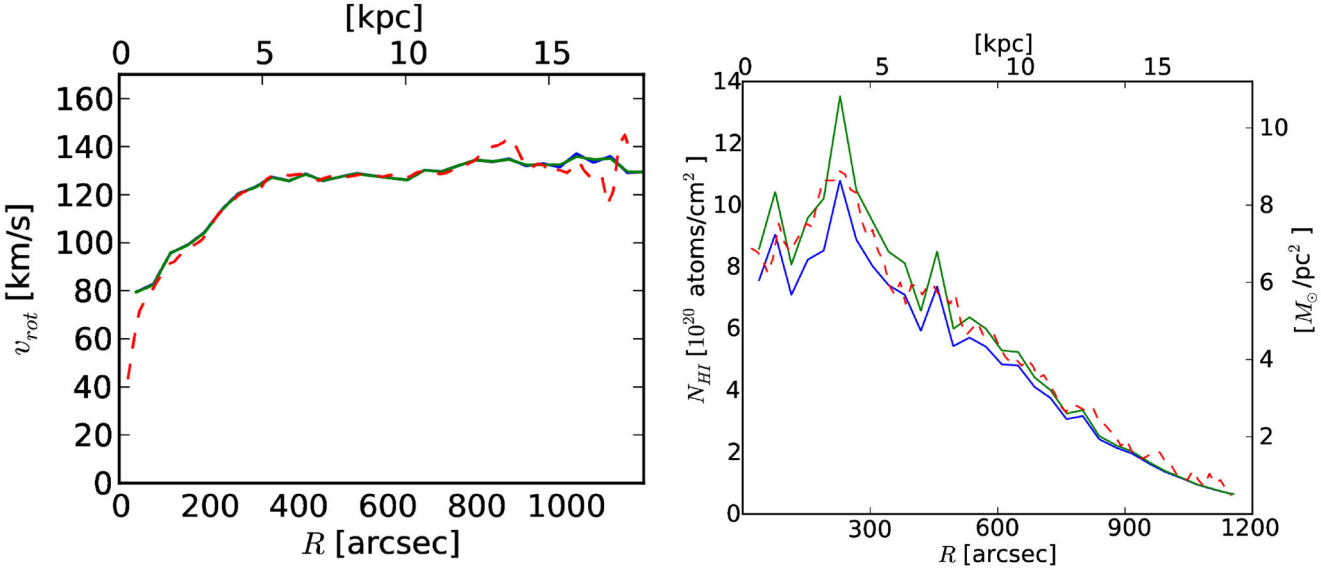


**Figure 6.** Kinematic and mass models for NGC 2403. The blue profiles represent the optically thin model. The green profiles are the self-absorption fit. The dashed red profiles represent the data from Sicking (1997).

Downloaded from https://academic.oup.com/mnras/article-abstract/464/1/21/2194606
by University of Groningen user
on 19 January 2018

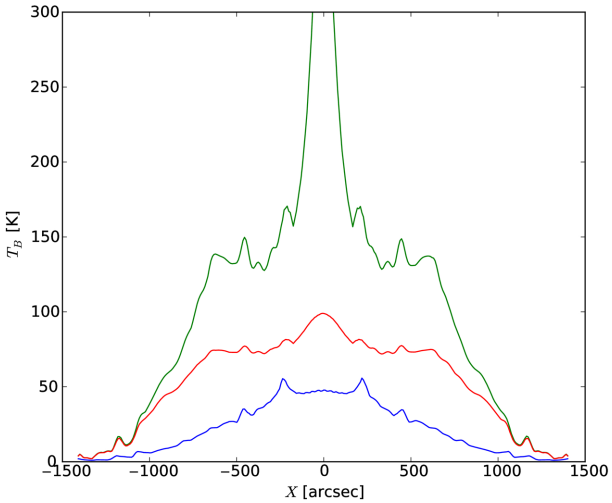


**Figure 7.** Maximum surface brightness along the major axis based on modelling for NGC 2403. The lower blue line is the galaxy at its normal inclination. The top green line is the optically thin case, as seen edge-on. The middle red line is the self-absorption case with a spin temperature of 100 K.

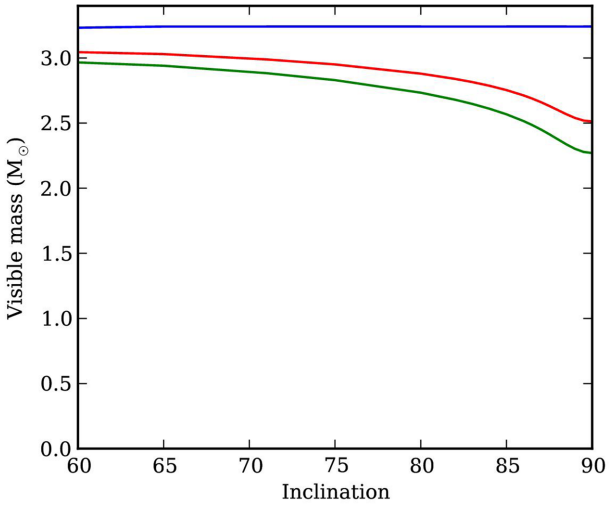


**Figure 8.** Visible H I in an edge-on model based on NGC 2403. The top blue line is the galaxy as if there is no self-absorption present. The bottom green line has self-absorption at $T_{\rm spin} = 100$ K. The middle red line is the self-absorption at $T_{\rm spin} = 150$ K.

the self-absorption model at $T_{\rm spin} = 100$ K, we see that the maximum surface brightness shows a clear plateau around 80 K with sharp edges. Comparing this with the galaxy observations in Paper I, the self-absorption clearly matches the data better than the optically thin model. Compared with the toy model from Section 3 of Paper I, the result is less dramatic than in fig. 2 in that article, where we applied a far higher face-on column density distribution than used here.

## 7 EFFECT OF INCLINATION ON THE VISIBLE MASS

Having established that an edge-on galaxy can easily hide a considerable fraction of its neutral hydrogen, we wish to test the relation between inclination and self-absorption. We test the effect of self-absorption on galaxies in the range of inclinations from 60–90°. We have selected $T_{\rm spin} = 100$ K and $T_{\rm spin} = 150$ K as the spin temperatures we wish to model and will produce an optically thin model at each inclination for comparison. We use the self-absorption results of NGC 2403 from Section 5 as the basis for all three models.

The results for this fit are shown in Fig. 8. It is clear that, in both cases, self-absorption is present at all inclinations. However, beyond an inclination of about 82°, the effects starts to increase drastically. Similarly to Paper I, we find that, for a spin temperature of 100 K, 30 per cent of the H I remains undetected. The milder case of a spin temperature of 150 K still has significant absorption, with ∼23 per cent of the H I going unseen.

A natural prediction from Fig. 8 would be that, in a statistical study, the edge-on galaxies would have a lower average H I mass than the face-on to moderately inclined galaxies. We have tried to investigate this by comparing the *K*-band magnitude (which is expected not to be much affected by inclination effects) with the apparent H I mass, using a combination of literature surveys. Unfortunately, we were unable to confirm or disprove the results, as there were too few edge-on galaxies in the available surveys with exact inclination measured. It is beyond the scope of this project to investigate this in more detail.

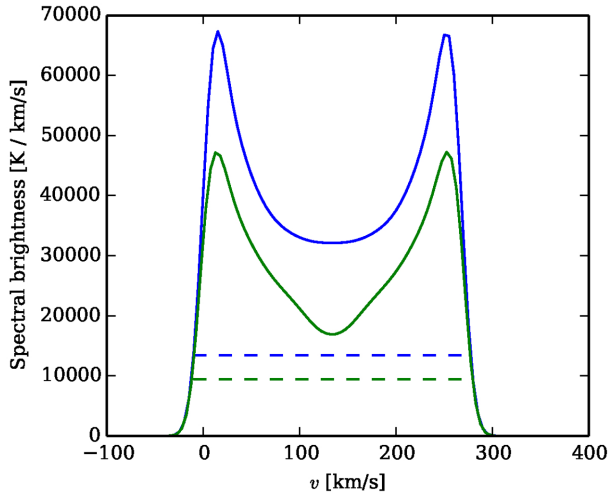


**Figure 9.** Impact on the width $w_{20}$ as measured from the spectra from an edge-on galaxy affected by optically thin (top, blue) and self-absorption with $T_{\rm spin} = 100$ K (bottom, green) cases.

## 8 THE BARYONIC TULLY–FISHER RELATION

Having established that edge-on galaxies can be affected by significant H I self-absorption, what is the effect on the baryonic Tully–Fisher (TF) relationship? The TF relation relates the dynamical mass of a galaxy to its luminosity and provides a test of theories of galaxy formation and evolution (Verheijen 1997; Bell & de Jong 2001). We use the two edge-on models from Section 6 as a basis for this analysis. The integrated spectra are shown in Fig. 9. The TF relation is based on the width $w_{20}$ of the profile at 20 per cent of the maximum in the integrated spectra (Tully & Fisher 1977). Clearly, this height varies drastically between the two cases, yet the difference between the two $w_{20}$ measurements is minimal. This is due to the sharp drop-off that both profiles show at the extremes, where self-absorption is less important. For the optically thin case, a value of 285.0 km s$^{-1}$ is found and for the self-absorption case, 291.0 km s$^{-1}$, an increase of only 2 per cent, is seen. We thus conclude that the $w_{20}$ parameter is not affected significantly by self-absorption.


Downloaded from https://academic.oup.com/mnras/article-abstract/464/1/21/2194606
by University of Groningen user
on 19 January 2018

The baryonic TF relation is, however, also based on the total baryonic mass $M_{\rm bar}$ and, as Fig. 9 clearly illustrates, self-absorption can affect that property significantly. The TF relation has not been well set, with various authors finding slopes between $M_{\rm bar} \propto V^3$ and $M_{\rm bar} \propto V^4$ (van der Kruit & Freeman 2011 and references therein). Although beyond the scope of this project, it will be interesting to see if the intrinsic scatter of the TF relation decreases when self-absorption of H I is taken into account.

## ACKNOWLEDGEMENTS

SPCP is grateful to the Space Telescope Science Institute, Baltimore, USA, the Research School for Astronomy and Astrophysics, Australian National University, Canberra, Australia, and the Instituto de Astrofisica de Canarias, La Laguna, Tenerife, Spain, for hospitality and support during short and extended working visits in the course of his PhD thesis research. He thanks Roelof de Jong and Ron Allen for help and support during an earlier period as visiting student at Johns Hopkins University and the Physics and Astronomy Department, Krieger School of Arts and Sciences for this appointment.

PCK thanks the directors of these same institutions and his local hosts Ron Allen, Ken Freeman and Johan Knapen for hospitality and support during many work visits over the years, of which most were directly or indirectly related to the research presented in this series of articles.

Work visits by SPCP and PCK have been supported by an annual grant from the Faculty of Mathematics and Natural Sciences of the University of Groningen to PCK accompanying of his distinguished Jacobus C. Kapteyn professorship and by the Leids Kerkhoven-Bosscha Fonds. PCK's work visits were also supported by an annual grant from the Area of Exact Sciences of the Netherlands Organization for Scientific Research (NWO) in compensation for his membership of its Board.

## REFERENCES

Allen R. J., Hamaker J. P., Wellington K. J., 1974, A&A, 31, 71
Allen R. J., Ivette Rodríguez M., Black J. H., Booth R. S., 2012, AJ, 143, 97
Begeman K. G., 1987, PhD thesis, Univ. Groningen
Bell E. F., de Jong R. S., 2001, ApJ, 550, 212
Binney J., Tremaine S., 1987, Galactic Dynamics. Princeton Univ. Press, Princeton, NJ
Bosma A., 1978, PhD thesis, Univ. Groningen
Braun R., Thilker D. A., Walterbos R. A. M., Corbelli E., 2009, ApJ, 695, 937
Dalcanton J. J. et al., 2009, ApJS, 183, 67
de Blok W. J. G., Walter F., Brinks E., Trachternach C., Oh S.-H., Kennicutt R. C., Jr, 2008, AJ, 136, 2648
Di Teodoro E. M., Fraternali F., 2015, MNRAS, 451, 3021
Draine B. T., 2011, Physics of the Interstellar and Intergalactic Medium. Princeton Univ. Press, Princeton, NJ
Foreman-Mackey D., Hogg D. W., Lang D., Goodman J., 2013, PASP, 125, 306
Fraternali F., Oosterloo T., Sancisi R., van Moorsel G., 2001, ApJ, 562, L47
Fraternali F., van Moorsel G., Sancisi R., Oosterloo T., 2002, AJ, 123, 3124
García-Ruiz I., Sancisi R., Kuijken K., 2002, A&A, 394, 769
Goodman J., Weare J., 2010, Comm. Appl. Math. Comp. Sci., 5, 65
Irwin J. A., 1994, ApJ, 429, 618
Irwin J. A., Seaquist E. R., 1991, ApJ, 371, 111
Irwin J. A., Seaquist E. R., 1993, ApJ, 415, 415
Józsa G. I. G., Kenn F., Klein U., Oosterloo T. A., 2007, A&A, 468, 731
Kamphuis P. et al., 2013, MNRAS, 434, 2069
Kamphuis P., Józsa G. I. G., Oh S.-H., Spekkens K., Urbancic N., Serra P., Koribalski B. S., Dettmar R.-J., 2015, MNRAS, 452, 3139
Krajnović D., Cappellari M., de Zeeuw P. T., Copin Y., 2006, MNRAS, 366, 787
O'Brien J. C., Freeman K. C., van der Kruit P. C., 2010, A&A, 515, A61
Olling R. P., 1995, AJ, 110, 591
Peters S. P. C., 2013, Galactus, Astrophysics Source Code Library. ascl.net
Peters S. P. C., van der Kruit P. C., Allen R. J., Freeman K. C., 2015a, MNRAS, in press (Paper I)
Peters S. P. C., van der Kruit P. C., Allen R. J., Freeman K. C., 2015b, MNRAS, in press
Press W. H., Teukolsky S. A., Vetterling W. T., Flannery B. P., 1992, Numerical Recipes in C, the Art of Scientific Computing, 2nd edn. Cambridge Univ. Press, New York, NY, USA
Rogstad D. H., Shostak G. S., 1971, A&A, 13, 99
Rogstad D. H., Lockhart I. A., Wright M. C. H., 1974, ApJ, 193, 309
Sancisi R., Allen R. J., 1979, A&A, 74, 73
Schoenmakers R. H. M., 1999, PhD thesis, Univ. Groningen
Sicking F. J., 1997, PhD thesis, Univ. Groningen
Spekkens K., Sellwood J. A., 2007, ApJ, 664, 204
Thi H., Vaz A., Vicente L., 2012, TOP: Off. Journ. Span. Soc. Stat. Oper. Res., 20, 190
Tully R. B., Fisher J. R., 1977, A&A, 54, 661
Tully R. B., Pierce M. J., 2000, ApJ, 533, 744
van der Hulst J. M., Terlouw J. P., Begeman K. G., Zwitser W., Roelfsema P. R., 1992, in Worrall D. M., Biemesderfer C., Barnes J., eds, ASP Conf. Ser. Vol. 25, Astronomical Data Analysis Software and Systems I. Astron. Soc. Pac., San Francisco, p. 131
van der Kruit P. C., Freeman K. C., 2011, ARA&A, 49, 301
Vaz A., Vicente L., 2007, J. Global Optimization, 39, 197
Vaz A., Vicente L., 2009, J. Global Optimization, 24, 669
Verheijen M. A. W., 1997, PhD thesis, Univ. Groningen
Walter F., Brinks E., de Blok W. J. G., Bigiel F., Kennicutt R. C., Thornley M. D., Leroy A., 2008, AJ, 136, 2563
Wiegert T. B. V., 2011, PhD thesis, Univ. Manitoba, Canada

## SUPPORTING INFORMATION

Additional Supporting Information may be found in the online version of this article:

**Appendix A.** Overview of input file layout and settings. (http://www.mnras.oxfordjournals.org/lookup/suppl/doi:10.1093/mnras/stw2099/-/DC1).

Please note: Oxford University Press is not responsible for the content or functionality of any supporting materials supplied by the authors. Any queries (other than missing material) should be directed to the corresponding author for the article.

This paper has been typeset from a TEX/LATEX file prepared by the author.

Downloaded from https://academic.oup.com/mnras/article-abstract/464/1/21/2194606
by University of Groningen user
on 19 January 2018